Materials Advances

ROYAL SOCIETY OF CHEMISTRY

PAPER

View Article Online
View Journal | View Issue

Cite this: *Mater. Adv.*, 2024, 5, 5958

What is the impact of plastic deformation on cytocompatibility of biodegradable Zn–Mg alloys?†

Daniel Wojtas,‡[abc] Klaudia Trembecka-Wójciga,‡[ad] Magdalena Gieleciak,[a] Agnieszka Bigos,[a] Kamil Brudecki,[e] Sylwia Przybysz-Gloc,[f] Romana Schirhagl,[c] Aldona Mzyk*[cg] and Anna Jarzębska *[a]

Research on biodegradable zinc requires thorough *in vitro* cytotoxicity screening as the developed materials are being proposed for various medical implants, including stents. This study investigates the endothelial cell response to a novel Zn–0.8Mg alloy produced *via* hydrostatic extrusion (HSE), aiming to showcase the impact of plastic deformation on the cytocompatibility of biodegradable zinc-based materials. In doing so, the MTT test for cell viability studies as well as confocal laser scanning microscopy (CLSM) imaging for cell morphology analysis were used. In addition, a cutting-edge diamond-based quantum sensing technique, *i.e.*, T1 relaxometry, was employed to reveal the nanoscale impact of ions on cells. It was demonstrated that the HSE-produced materials exhibited a 10-fold decrease in grain size, microstructural homogenization, and consequently more uniform degradation compared to hot extruded, coarse-grained materials. Despite these differences, the MTT and CLSM data did not show any drastic discrepancies between the endothelial cell response to any of the investigated materials. However, T1 relaxometry measurements indicated that plastic deformation might influence the cytocompatibility of biodegradable zinc-based materials, as evidenced by significant intracellular free radical production in endothelial cells exposed to ions released from the Zn–0.8Mg HSE alloy surface. Overall, no adverse effects of plastic deformation on the cytocompatibility of zinc-based materials were found as free radical generation may play a beneficial role in endothelial cell function, suggesting a complex interaction between material degradation and cellular response.

Received 1st February 2024,
Accepted 29th May 2024

DOI: 10.1039/d4ma00098f

rsc.li/materials-advances

1. Introduction

Ischemic heart disease constitutes the leading cause of global mortality. The disease is a clinical manifestation of atherosclerosis, initiated by the accumulation of fatty and/or fibrous substances in the innermost layer of arteries, known as the intima.[1] Percutaneous coronary intervention, performed with the implantation of a stent, is the most common and effective treatment for atherosclerosis. With respect to materials used in the production of stents, two generations of permanent systems, *i.e.*, bare-metallic stents and drug eluting stents, have been designed, developed, and perfected for years. However, several stent-related complications, including injury, late stent thrombosis, restenosis, neo-atherosclerosis, and the lack of normal vessel reactivity continue to pose significant risks to patient safety.[2] This is why a novel group of stent-intended materials, *i.e.*, biodegradable metals, alloys, and composites has come to the fore. In principle, upon fulfilling their purpose *i.e.*, supporting a diseased vessel, they would completely break down leaving no harmful residues at the site of implantation.[3] Iron-, magnesium-, and zinc-based materials tend to degrade under biological conditions, thus they have been widely investigated as potential replacements for both bare-metallic and drug-eluting stents.

[a] *Institute of Metallurgy and Materials Science, Polish Academy of Sciences, Reymonta 25, 30-059 Kraków, Poland. E-mail: a.jarzebska@imim.pl*
[b] *Department of Pathophysiology, Faculty of Medicine, Masaryk University, Kamenice 753/5, 625 00 Brno, Czechia*
[c] *Department of Biomedical Engineering, University of Groningen, University Medical Center Groningen, Antonius Deusinglaan 1, 9713AW, Groningen, The Netherlands. E-mail: aldonamzyk@googlemail.com*
[d] *Faculty of Chemical Engineering and Technology, Cracow University of Technology, Warszawska 24, 31-155 Kraków, Poland*
[e] *Institute of Nuclear Physics, Polish Academy of Sciences, Radzikowskiego 152, Krakow, 31-342, Poland*
[f] *Institute of High Pressure Physics, Polish Academy of Sciences, Warszawa, Poland*
[g] *Department of Health Technology, Danish Technical University, Ørsteds Plads, DK-2800 Kongens Lyngby, Denmark*

† Electronic supplementary information (ESI) available. See DOI: https://doi.org/10.1039/d4ma00098f

‡ These authors contributed equally.

From the point of view of biodegradation, zinc is situated between iron (corroding too slowly) and magnesium (corroding too rapidly), as it corrodes with an optimal ratio. The element plays a crucial role as a micronutrient in human metabolism, catalyzing over 100 enzymes, facilitating protein folding, and contributing to the regulation of gene expression.[4] Zinc also promotes bone formation and its recovery, interacts with nucleic acid molecules, and regulates apoptosis as well as gene expression. The scientific exploration of zinc as a potential biomaterial is therefore justified. So far, casting and conventional wrought procedures have been the most frequently utilized processes in the manufacture of biodegradable zinc-based alloys and composites.[5] At the same time, a variety of advanced processing methods, including directed solidification casting,[6] mechanical alloying,[7] or additive manufacturing[8] have also been exploited to produce zinc-based materials meeting the stringent criteria for biodegradable implants. The ultimate goal of any fabrication method is to improve the unfavorable mechanical characteristics of pure zinc without compromising its corrosion behavior. Hydrostatic extrusion (HSE), an unconventional plastic deformation process, results in a remarkable improvement of strength, provided that multi-step processing is undertaken.[9–11] While Zn, as well as Zn–0.5Mg, Zn–1Mg, and Zn–1.5Mg alloys produced *via* HSE, have been extensively analyzed concerning their microstructure, crystallographic texture, and mechanical properties, the biological behavior of biodegradable HSE-processed zinc remains largely unexplored.

Despite many promising trials, including *in vivo* testing, the biocompatibility of zinc has continued to be a matter of debate.[12] It is essential to address this issue by complex cytotoxicity screenings, striving for metanalyses, or making use of novel protocols, and methods. Thus, within this study, a pioneering effort to examine the cytotoxicity of zinc-based materials processed *via* HSE was made. The investigation employs T1 relaxometry, alongside the MTT assay as well as qualitative and quantitative confocal laser scanning microscopy (CLSM), to assess the impact of ions released from the surfaces of plastically deformed zinc/zinc alloy on cells. T1 relaxometry, a special mode of diamond-based quantum sensing whose principles can be found elsewhere,[13] has been successfully applied to check the nanoscale impact of zinc ions on endothelial cells.[14] It has been revealed that Zn^{2+} released from biodegradable samples induces the intracellular formation of free radicals and that the overload of zinc ions in the cell environment results in the excessive production of reactive oxygen/nitrogen species and cell death. In biomaterial studies, T1 relaxometry has also been used to reveal whether free radicals are generated in lung epithelial cells exposed to nickel, titanium, and nitinol.[15] It is worth mentioning that T1 relaxometry has already shown great potential in monitoring the free radical generation during *e.g.*, chemical reactions,[16] shear stress in endothelial cells,[17] response of bacteria to antibiotics,[18] or upon viral infections.[19] The versatility of the technique has been demonstrated while detecting free radicals in various cell cultures, including the already-mentioned epithelial[15] and endothelial[17] cells, as well as dendritic cells,[20] HeLa cells,[21] macrophages,[22] granulosa cells,[23] or sperm cells.[24] The method enables measurements in single-cell organelles, such as mitochondria,[25] or particular cellular locations, such as acrosomes.[26] The versatility of T1 relaxometry, demonstrated in detecting free radicals across various cell cultures, showcases unparalleled potential in biomaterial studies.

Within the present study, a novel approach to examining the cytocompatibility of zinc has been adopted. The main goal was to explore the influence of plastic deformation on the biological behavior of zinc-based materials. As a consequence, by utilizing T1 relaxometry, new insights into the nanoscale effects of zinc ions on endothelial cells were gained. So far, research on biodegradable metals has been primarily focused on their bulk properties and general biocompatibility, with no attention given to the nanoscale effects the materials may induce. Our investigation not only expands the application of T1 relaxometry but also addresses the cytocompatibility of zinc/zinc alloy at the nanoscale.

2. Materials and methods

2.1. Zinc-based materials

Two different materials, *i.e.*, pure Zn, and Zn–0.8Mg, were examined within the present study upon gravity casting and subsequent plastic deformation, realized *via* two different routes. The starting materials were zinc of high purity (99.99%) and magnesium (99.9%). First, they were melted at 650 °C under argon atmosphere and cast into steel molds. Afterwards, hot extrusion (HE) followed by HSE was performed to meet the requirements imposed on biodegradable implants from the point of view of their mechanical strength.[27] In fact, our previous studies[10,11] revealed the combination of HE and HSE results in significant improvements of mechanical properties that zinc and its alloys exhibit. First, the as-cast materials were subjected to HE at 250 °C with a reduction (R) of 5.8. Parts of the obtained rods were sliced and stored for experiments, while the remaining pieces were subjected to HSE. The operation was conducted at room temperature in three consecutive stages, yielding a cumulative true strain (ε) of 3.6.

Prior to microstructural characterization described herein, the material samples were cut, ground with the use of silicon carbide papers ranging in grit from 220 to 7000, polished with diamond suspensions (1 μm and 0.25 μm of diamond particle size), and electro-polished with an electrolyte containing distilled water, ethanol, butoxyethanol, and sodium thiocyanate. In the case of the cell-material interaction studies, zinc extracts, described hereunder were employed.

2.2. Extract formation

Due to degradability of zinc and its alloys, cell culture media containing ions released from the surfaces of zinc-based materials were prepared, stored, and used for cell response studies. Zinc/alloy discs were sterilized with UV light for 1 hour, placed into 12-well plates, and immersed in the endothelial basal medium (EBM, Lonza) at a medium-to-sample ratio of

1.25 mL cm^{-2}. After 24 and 48 hours of incubation (at 37 °C and 5% CO_2), the resulting solutions, henceforth referred to as extracts, were collected and stored at −20 °C for further use. In general, the extracts are a mixture of cell culture medium and metal ions, as described in our previous study.[14] Within the present article, for the sake of brevity, we call the harvested extracts simply ''zinc extracts'' even though for the Zn–0.8Mg alloy, they might contain some minute concentration of the alloying addition. Prior to cell-response investigations, three different concentrations of extracts upon serial dilution with cell culture medium were studied, *i.e.*, 20%, 60% and 100% (no dilution).

2.3. Fluorescent nanodiamonds

For T1 relaxometry measurements, fluorescent nanodiamond particles (FNDs), having a mean hydrodynamic diameter of 70 nm and exhibiting a flake-like morphology were used. They were sourced from Adamas Nanotechnologies, NC, USA, and according to the manufacturer, were produced by the high-pressure high-temperature method followed by grinding. During post-production, FNDs are irradiated with 3 MeV electrons at a fluence of 5×10^{19} ecm^{-2} and then annealed above 700 °C.[28] This results in the incorporation of approximately 500 nitrogen vacancy (NV^-) centers in a single FND particle. The concluding step in their fabrication process involves treatment with oxidizing agents, leading to an oxygen-terminated surface. Recognized for their unparalleled biocompatibility, FNDs also demonstrate stable charge and everlasting fluorescence properties.[29] For the T1 relaxometry measurements, FNDs at a concentration of 2 μg mL^{-1} were employed.

2.4. Cell culture

HUVECs (CC2519, Lonza), obtained by the courtesy of the Endothelial Facility, University of Groningen, were utilized for cell response studies. HUVECs were cultured in the EGM-2MV solution (CC3202, Lonza), composed of EBM-2 Basal Medium (CC3156, Lonza), and supplemented with EGM-2 MV growth factors (CC4147, Lonza). Cell cultures were maintained at 37 °C and 5% CO_2 until 80–90% confluency was reached.

2.5. Mass change test

Mass change tests were performed to check how biodegradable samples behave in complete EBM. The mass change is defined as the difference between the initial mass of the sample and its mass after a period of incubation, following subsequent removal of corrosion products. It could be either a loss (corresponding to the material undergoing corrosion) or an increase (ascribed to the precipitation of corrosion products). The complete EBM was employed for the mass change tests for all investigated materials. The ratio of medium to surface was 1.25 mL cm^{-2}, and similarly to the extract production, the duration of the experiment was set to either 24 or 48 hours. Consequently, the corroded samples were rinsed with distilled water and treated with a solution of 1.5 M chromic acid to guarantee the removal of the corrosion layer/products. Finally, the samples were dried and weighed. For each of the time point set, three different specimens were tested, and the results were averaged.

2.6. Mass spectrometry

Prior to mass spectrometry analysis, the extracts were mineralized using ultra-pure nitric acid (Merck, 65%) and a microwave digestion system (PreeKem). Subsequently, they were diluted to a 2% nitric acid matrix using ultra-pure water (Merck Milli-Q). The mineralized extracts were transferred into a mass spectrometer. Zn and Mg concentrations were determined by a triple quadrupole inductively coupled plasma mass spectrometer (ICP-MS, Agilent 8900). The spectrometer operated in a dual-quad mode with a collision-reaction cell and helium flow at a rate of 4.5 L per minute. Calibration was performed using calibration solutions of selected elements specifically designed for mass spectrometry (ROTH). Quality control was conducted using reference materials of human blood, namely, Seronorm™ - trace elements whole blood. During the presented study, two measurements of the reference material were carried out. For Zn, the obtained results were 6.77 ± 0.20 mg L^{-1} and 6.75 ± 0.20 mg L^{-1}, while the certified value was 6.20 ± 1.20 mg L^{-1}. For Mg, the results were 24.55 ± 0.74 mg L^{-1} and 24.53 ± 0.74 mg L^{-1}, while the certified value was 26.7 ± 5.4 mg L^{-1}. The obtained Zn and Mg results aligned with the certified values.

2.7. Scanning electron microscopy

Alterations in the microstructure of the analyzed zinc-based materials induced by two different deformation routes were analyzed employing an FEI Quanta 3D scanning electron microscope (SEM), set to the backscatter electron (BSE) mode. In addition, orientation mapping with the use of the electron backscatter diffraction (EBSD) technique was also carried out to enable quantitative microstructural analysis of the materials. The EBSD maps were gathered by adjusting their size and the step size for each of the samples individually (840 μm × 840 μm and 0.5 μm for Zn HE; 368 μm × 368 μm and 0.27 μm for Zn–0.8Mg HE; 155 μm × 155 μm and 0.25 μm for Zn HSE; 105 μm × 105 μm and 0.12 μm for Zn–0.8Mg HSE). Upon data collection, microstructural parameters, such as mean grain size and grain boundary density were computed by using the TSL 7.0 software. Grain boundary density was calculated as the ratio of a specific grain boundary divided by the EBSD map area. For low angle boundaries, the misorientation angle (θ) was set between 2 and 15°, whereas for high angle grain boundaries, θ was set as greater than 15°. The ImageJ software was used to characterize the Mg_2Zn_{11} intermetallic phase in detail. The density of the Mg_2Zn_{11} phase was determined by analyzing BSE images. This involved counting the number of the distinguished intermetallic phase identified by phase contrast using the ImageJ, and dividing this count by the total area of the BSE image. To ensure statistical reliability, four images captured at the same magnification from various location on the samples were used to calculate the average value. For a more extensive description of the EBSD-derived parameters, readers are encouraged to reach out to *e.g.*, our previous reports.[10,30,31]

2.8. Corrosion properties

The corrosion behavior of Zn and Zn–0.8Mg alloys (HE and after HSE) was studied based on potentiodynamic polarization tests in Hanks' balanced salt solution (HBSS, pH = 7.4) corresponding to the blood plasma ionic composition.[32] The samples were immersed in the solution and kept at 37 °C for 1 and 30 days prior to the electrochemical tests. All the experiments were carried out in a three-electrode setup using an AUTOLAB PGSTAT302N potentiostat/galvanostat (supplied with the NOVA 2.14 software) in a thermostated electrochemical cell (at 37 °C). The working surface of Zn and Zn–0.8Mg cylindrical samples (0.2 cm^2) was abraded on SiC-based papers up to 7000 grit and polished with a diamond suspension before each measurement. The saturated calomel electrode (SCE) placed in a Luggin capillary and platinum spiral were used as the reference and the counter electrode, respectively. The open circuit potential (OCP) was monitored for one hour. Then, the polarization curves were registered in the potential range ±120 mV with respect to the OCP, with a scan rate of 0.001 V s^{-1}. The measured data were analyzed using the Tafel extrapolation method, and the corrosion current density (i_{corr}, μA cm^{-2}), corrosion potential (E_{corr}, mV), slopes of anodic and cathodic polarization curves (β_a, β_b), corrosion rate (CR, mm $year^{-1}$), and polarization resistance (R_p, Ohm) values were determined using NOVA 2.14.

2.9. X-ray diffraction

The phase composition of the studied materials was analyzed by means of X-ray diffraction (XRD) using a Bruker D8 Discover diffractometer equipped with a Co anode. The analysis employed specific parameters: a voltage of 40 kV, a current of 40 mA, an angular step of $2\theta = 0.02^\circ$, and an acquisition time of 2 s per step. Upon spectrum collection, phase indexing was conducted using the DIFFRAC.EVA (Bruker) software.

2.10. Confocal laser scanning microscopy

The interactions between the endothelial cells and the tested materials were assessed after 4 hours of cell exposure to differently concentrated zinc extracts. Before image acquisition, HUVECs were fixed using a 3.7% paraformaldehyde solution for 10 minutes and permeabilized with a 0.1% solution of Triton X-100 (Sigma) for 7 minutes. Afterward, the cells were rinsed with fresh phosphate-buffered saline (PBS). The fixed HUVECs were stained with FITC-phalloidin (Sigma) for 35 minutes and DAPI (Sigma) for 5 minutes, allowing visualization of the F-actin structural fibers and the nuclei, respectively. The final step involved threefold washing of the cells with PBS to clear away any dye leftovers. A Stellaris 8 Leica Microsystems CLSM was used for imaging. The gathered images were refined using the LAS X software, and for a more in-depth quantitative breakdown of the CLSM-obtained information, ImageJ was employed. The cell shrinkage ratio was computed using extract-free cells as a reference.

2.11. MTT assay

Viability of cells exposed to zinc extracts was determined based on the standard MTT assay. For each concentration tested (20%, 60%, and 100%), six replicates were set up. As a comparison, extract-free cells and cells containing 10% dimethyl sulfoxide (DMSO) were used as negative and positive controls, respectively. After 4 hours of incubation, an aqueous solution of tetrazolium salt – specifically 3-(4,5-dimethylthiazol-2-yl)-2,5-diphenyltetrazolium bromide (Sigma) – at a concentration of 5 mg mL^{-1}, was added to each well. After an additional incubation period of 3 hours, the medium + MTT mixture was discarded, and the precipitated formazan crystals were dissolved using DMSO. Subsequently, the plates were gently agitated in the dark for 2–3 minutes. Finally, the resultant color intensity, which directly correlates with cell viability, was quantified using a microplate reader (Biotek Instruments) set to a wavelength of 570 nm.

2.12. T1 relaxometry

HUVECs were seeded at a density of 1×10^4 cells per mL in special four-compartment dishes (CELLview). The cells were incubated with 2 μg mL^{-1} of FNDs for 2 hours at 37 °C and 5% CO_2. Afterward, the cells were exposed to either 100%, 60%, or 20% extracts for 4 hours. The concentration of free radicals was estimated based on T1 relaxation curves recorded during tracking of intracellularly distributed nanodiamond sensors. For this purpose, a custom-made diamond magnetometer,[33] a modified version of a CLSM was used. All the T1 relaxometry measurements were conducted under static conditions at room temperature. The experiments were performed in six replicates for each variant.

2.13. Statistical analysis

The statistical significance of the data was assessed using GraphPad Prism v. 10 software. To compare the differences among the analyzed probes, a two-way ANOVA with Tukey's test was employed for multiple comparison tests, and a threshold of $p < 0.05$ was selected for statistical significance.

3. Results

3.1. Microstructure

Fig. 1 depicts the microstructures of the analyzed materials obtained using the BSE mode in SEM along with EBSD-derived orientation maps. The HE-processed zinc (Fig. 1a) was characterized by a coarse-grained microstructure with well-developed, nearly-equiaxial grains and clearly visible high-angle grain boundaries (HAGBs), depicted as black lines on the orientation maps. Alloying with magnesium (Fig. 1b) led to the formation of a eutectic mixture composed of α-Zn and the intermetallic phase Mg_2Zn_{11}. The presence of this eutectic contributed to a ten-fold reduction in the mean grain size of the alloy compared to pure zinc. Moreover, it may be observed that Mg_2Zn_{11} clusters tended to form in proximity to HAGBs.

The HSE process resulted in more pronounced grain refinement than that provoked by HE. HSE also brought about substantial downsizing of the intermetallic phase and its even redistribution within the matrix. The area fraction of the

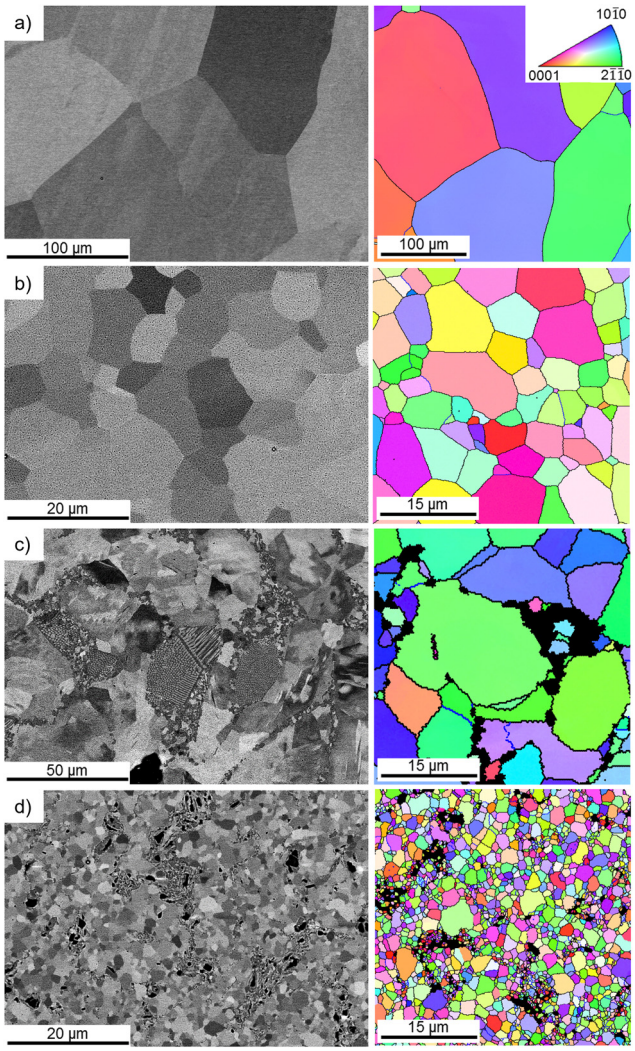

Fig. 1 SEM/BSE images and orientation maps of (a) Zn HE, (b) Zn HSE, (c) Zn–0.8Mg HE, (d) Zn–0.8Mg HSE. Black areas on the orientation maps of the Zn–Mg alloys indicate the presence of the intermetallic phase and were excluded from the analysis. Black and blue lines on the orientation maps represent HAGBs and LAGBs, respectively. The color coding of the orientation map along ED is based on the triangle depicted in the upper left corner of the figure. Please pay attention to the different scale markers.

Mg_2Zn_{11} phase, calculated with the use of the ImageJ software, was approximately 30% lower for the HSE-treated alloy in comparison to that of HE. The mean area of the intermetallic phase decreased with the introduction of HSE, whereas its density was markedly higher in the HSE-treated alloy. It is also worth mentioning that unlike the deformation triggered by HE, HSE caused the formation of numerous structural defects, expressed herein as low angle grain boundaries (LAGBs). A summary of microstructural features for all investigated materials is shown in Table 1, whereas LAGBs are better visible as blue lines on the orientation maps, illustrated in Fig. S1 (ESI†).

3.2. Phase composition

The XRD spectra collected for all of the examined materials are illustrated in Fig. 2. The presence of many distinct, sharp peaks, assigned to α-Zn, was confirmed. Upon closer inspection, it can be seen that the Zn–0.8Mg alloys, regardless of the deformation path, contained also the Mg_2Zn_{11} intermetallic phase. Compared to pure zinc, both alloys showed a significantly higher intensity of the XRD peak corresponding to the (101) plane of zinc. This observation may be related to a strong crystallographic texture, which is a characteristic phenomenon of plastically deformed materials.[30]

3.3. Mass change test

Mass change tests were performed to determine if dissolution (mass loss) or corrosion product formation (mass increase) predominates during the immersion of zinc samples in complete EBM. The results, referenced to the initial sample mass, are illustrated in Fig. 3. Regardless of whether the corrosion layers/products were removed or not, the HE materials exhibited a significant variability in mass change values as indicated by the variations in the box plots. This suggests that both zinc and Zn–0.8Mg processed by HE degrade irregularly. In fact, some HE samples exposed to EBM experienced a mass loss (an indicative of dissolution), while others were already covered with corrosion products/layers (indicative of corrosion protection). Due to these large discrepancies in mass change among the HE materials, no statistical significance was observed between the HSE and HE specimens. However, the HSE materials generally demonstrated more uniform degradation behavior. The differences in mass change within the same set of the HSE materials were minimal as evidenced by the consistent appearance of the box plots. In addition, a protective layer formation or precipitation of corrosion products was viewed on the majority of the HSE surfaces. Notably, the HSE-treated Zn–0.8Mg alloy immersed in EBM for 48 hours was the only one that exhibited a mass loss. Stable degradation of the HSE materials was further confirmed upon the chromic acid-assisted removal of corrosion products, with mass loss ranging approximately between 0.15 and 0.3 mg. The differences in mass loss (after clearance of the corrosion products/layers) between the HSE and HE materials were statistically significant, except for the Zn–0.8Mg alloy exposed to EBM for 48 hours. This suggests that under biological conditions, the HE specimens may degrade in an unstable fashion.

The quantitative mass change test was further supported by SEM observations, which confirmed that the HSE materials tend to dissolve more homogeneously than the HE materials (Fig. 4). Such a tendency was particularly notable when removal of corrosion products/layers was undertaken. In the case of the HSE-treated materials, uniformly distributed corroded pits were observed, and their number increased with prolonged immersion. For the HE-processed materials, more localized corrosion occurred, and the corrosion products/layers were more irregular. Additionally, the EDS analysis (data not shown) revealed no significant differences in the chemical composition of the corrosion products between HSE and HE materials. Elements such as Zn, O, Cl, P, C, Mg and Ca were detected, indicating a possible formation of *e.g.*, ZnO, $ZnCl_2$, $Zn(OH)_2$, $ZnCO_3$, $Zn_3(PO_4)_2$, $Zn_5(CO_3)_2(OH)_6$, $CaCO_3$, or $Ca_3(PO_4)_2$.[34,35]

Table 1 Microstructural features of the investigated materials

	Zn HE	Zn HSE	Zn–0.8Mg HE	Zn–0.8Mg HSE
Mean grain size (α-Zn) (μm)	279 ± 117	9 ± 3	20 ± 10	2.1 ± 1
HAGB density (1/μm)	0.06	0.40	0.14	1.43
LAGB density (1/μm)	0.01	0.04	0.03	0.21
Mg_2Zn_{11} area fraction	—	—	0.24 ± 0.02	0.16 ± 0.02
Mean area of Mg_2Zn_{11} (μm^2)	—	—	468 ± 126	203 ± 112
Density of Mg_2Zn_{11} (1/μm)	—	—	0.006 ± 0.002	0.014 ± 0.004

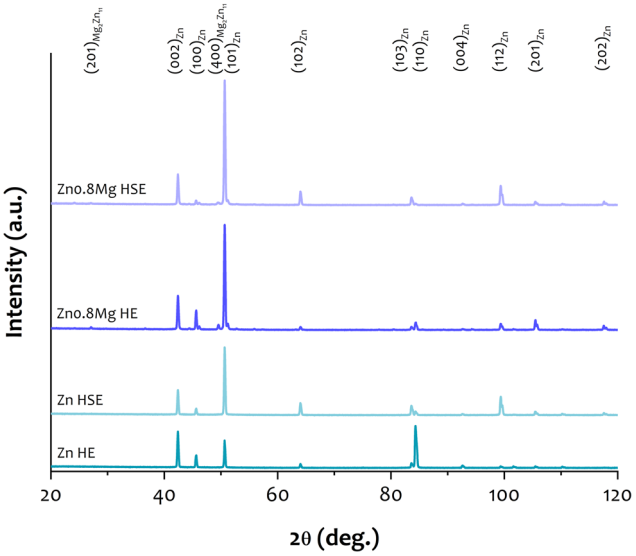

Fig. 2 XRD patterns of Zn and Zn–0.8Mg processed by HE and HSE.

3.4. Ion concentration

According to the ICP-MS data listed in Table 2, the concentration of zinc in the Zn HE extracts was substantially greater than in the Zn HSE extracts, regardless of the immersion time. A similar trend was observed for the alloys, yet only for the 24-hour experiment. Overall, there was an increase in the ion concentration with longer incubation times in most cases. The Zn–0.8Mg HE alloy was an exception, as both Zn and Mg concentrations decreased after a 48-hour immersion. This phenomenon may be attributed to the formation of the passive layer on the material surface, protecting it from further degradation or is an indicative of material undergoing unstable dissolution. In fact, the concentration of Zn in the Zn–0.8Mg HE extract upon a 48-hour test was nearly half that of the Zn–0.8Mg HSE, which exhibited relatively uniform degradation. It is also noteworthy that the concentration of Mg in the extracts produced after 24 hours of immersion of the Zn–0.8Mg HSE was lower (258.9 ± 7.8 mg L^{-1}) than in the EBM (262.8 ± 7.9 mg L^{-1}). This suggests that the material attracted magnesium present in the medium, possibly leading to the development of Mg-rich precipitates on its surface.

3.5. Corrosion properties

To gain deeper insight into the degradation of Zn and Zn–0.8Mg obtained *via* HE and HSE, their corrosion properties were evaluated through potentiodynamic tests after immersion for 1 and 30 days. Despite variations in plastic deformation route and chemical composition of materials, the overall character of the potentiodynamic curves remained consistent, as seen in Fig. 5a. After 1 day of immersion, slightly lower corrosion potential was observed for the Zn–0.8Mg alloys compared to pure Zn, suggesting that the intermetallic phase could influence corrosion properties.[36] This observation is based on the data in Table 3, presenting the electrochemical parameters calculated through Tafel extrapolation of potentiodynamic curves. The corrosion current density values fell within a similar range, with a slight advantage for the Zn–0.8Mg HE, indicating a slower degradation rate compared to the other investigated materials. Overall, an early-stage corrosion behavior appeared to be similar for all the examined materials. As time progressed, more pronounced differences between the materials became apparent. Except for the Zn HE, the electrochemical potential shifted towards more positive

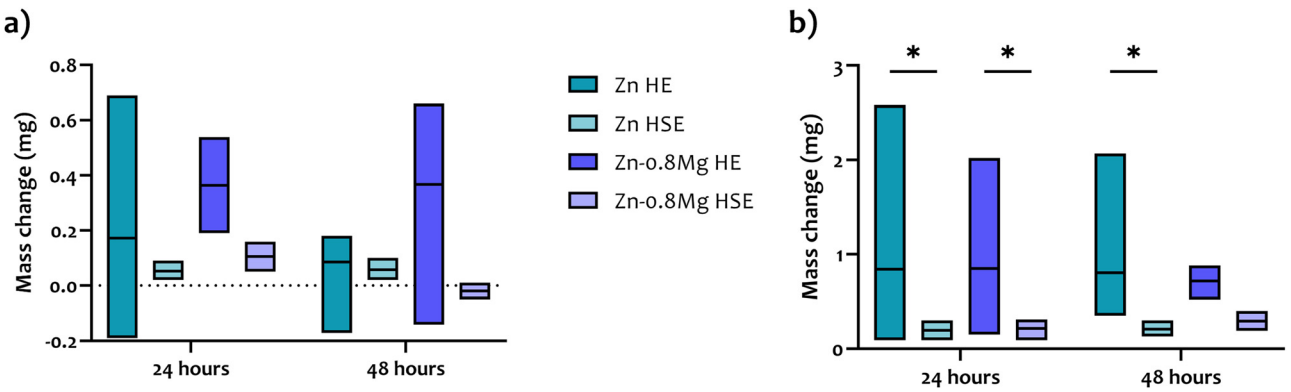

Fig. 3 Post-immersion mass change (a) with corrosion products and (b) after removal of corrosion products with chromic acid.

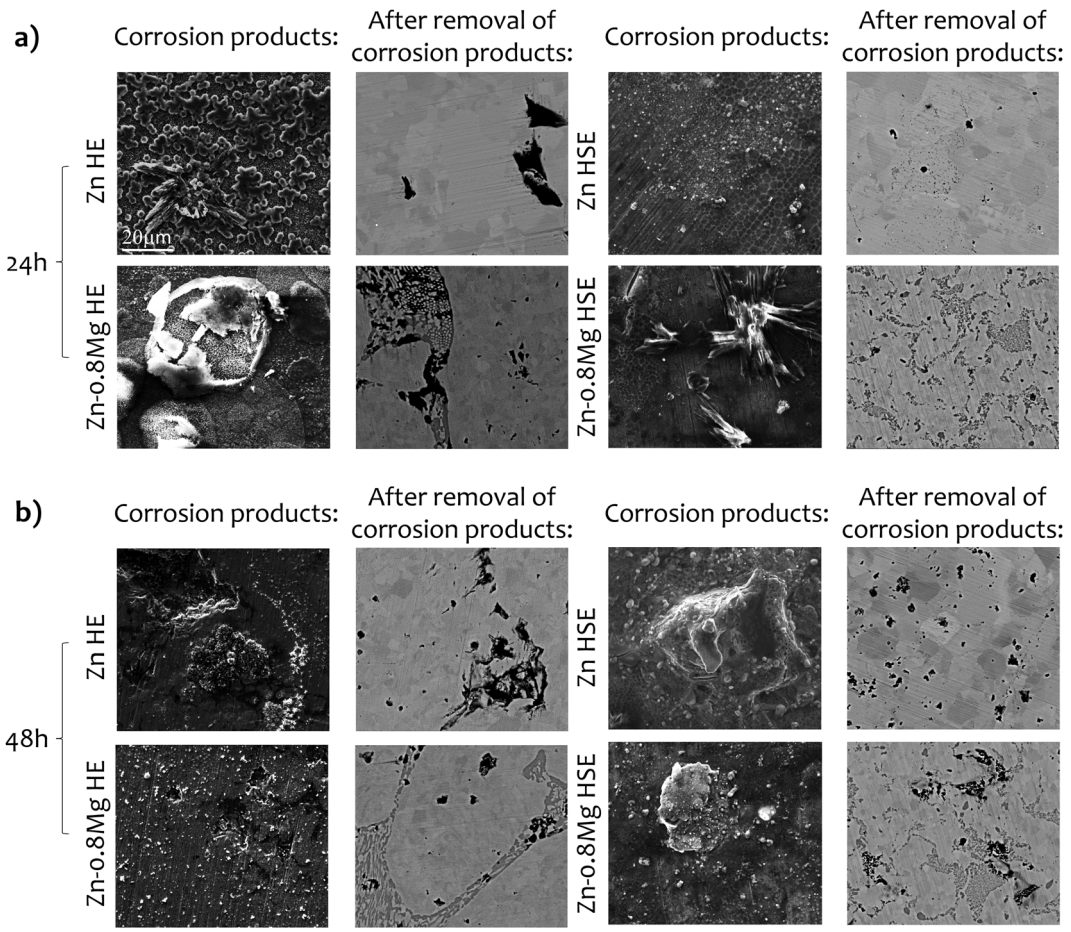

Fig. 4 SEM/BSE images of material surfaces with and without corrosion products observed after (a) 24 hours and (b) 48 hours of immersion in EBM. The scale bar, denoting 20 μm, is inserted in the Zn HE 24 h image and remains consistent across all images.

Table 2 Concentration of ions in the extracts revealed by the ICP-MS technique

	Concentration of Zn (mg L^{-1})		Concentration of Mg (mg L^{-1})	
	24 h	48 h	24 h	48 h
EBM (ref.)	0.04 ± 0.001	0.04 ± 0.001	262.8 ± 7.9	262.8 ± 7.9
Zn HE	47.2 ± 1.4	76.3 ± 2.3	—	—
Zn HSE	40.9 ± 1.2	60.9 ± 1.8	—	—
Zn–0.8Mg HE	56.9 ± 1.7	30.6 ± 0.9	289.6 ± 8.7	265.0 ± 8.0
Zn–0.8Mg HSE	42.9 ± 1.3	60.6. ± 1.8	258.9 ± 7.8	270.0 ± 8.1

values, implying the formation of a protective corrosion layer. Interestingly, in comparison to the HSE materials, the current densities evaluated for their HE counterparts increased considerably, resulting in significantly higher corrosion rates. This suggests that the corrosion layer formed on the HSE-deformed materials was more compact and protective than that on the HE-treated materials. It should be noted that the Zn HSE upon 30-day immersion demonstrated the lowest anodic current, implying the most compact protective layer.[35] In the case of the Zn–0.8Mg HSE alloy, more diverse corrosion layer is expected to cover the material due to the presence of the intermetallic phase. The formation of *e.g.*, MgO was thus possible, what in turn might have increased the material degradation.[27,37]

3.6. Cell morphology

Fig. 6 and 7 depict CLSM-derived morphology of HUVECs treated with extracts collected from the HE and HSE materials, respectively. Upon initial inspection, two major observations can be made. Firstly, irrespective of the processing path, the material, or the extract concentration that was used, cell viability significantly decreased when HUVECs were exposed to media harvested upon a 48-hour incubation with zinc-based specimens. Secondly, the majority of the analyzed 20% extracts

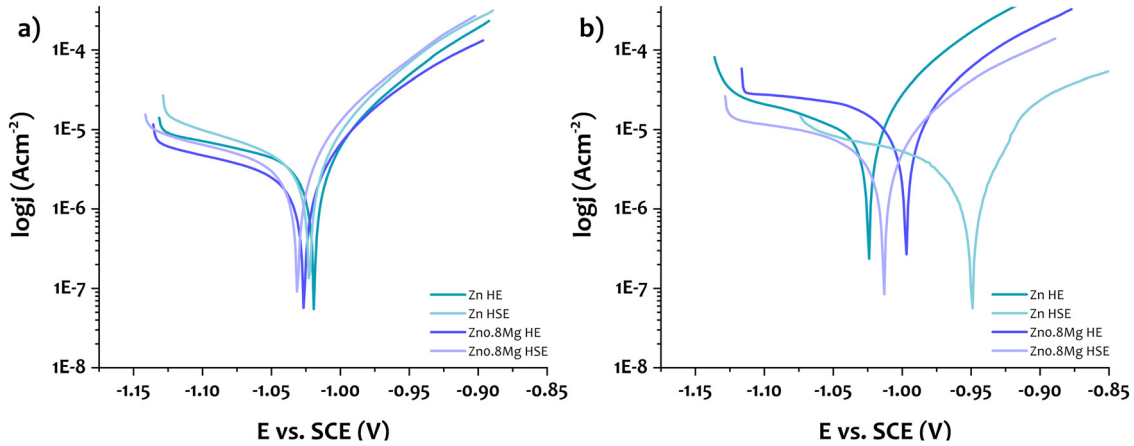

Fig. 5 Potentiodynamic curves of the investigated materials after immersion in HBSS for (a) 1 day and (b) 30 days.

Table 3 Electrochemical corrosion data obtained from polarization curves of the investigated materials. OCP – open circuit potential, E_{corr} – corrosion potential, J_{corr} – corrosion current, CR – corrosion rate, R_p – polarization resistance, β_a – anodic slope, β_c – cathodic slope

	Immersion days	OCP (V)	E_{corr} (V)	J_{corr} (μA cm^{-2})	CR (mm year^{-1})	R_p (Ω)	β_a (V dec^{-1})	β_c (V dec^{-1})
Zn HE	1	−1.012	−1.019	3.6	0.053	29888	0.06	0.26
	30	−1.019	−1.024	11.1	0.164	11037	0.08	0.19
Zn HSE	1	−1.010	−1.023	3.9	0.058	25035	0.06	0.18
	30	−0.934	−0.949	4.7	0.071	39217	0.13	0.28
Zn–0.8Mg HE	1	−1.018	−1.026	2.6	0.039	45720	0.07	0.25
	30	−1.000	−0.997	16.9	0.254	9056	0.08	0.45
Zn–0.8Mg HSE	1	−1.022	−1.031	3.7	0.056	32155	0.07	0.23
	30	−1.002	−1.013	6.4	0.096	22950	0.09	0.32

did not lead to any drastic changes in cell activity, as a nearly complete monolayer was still viewed in most of those cultures. Obviously, the most striking alterations in cell morphology were noticed for HUVECs exposed to the 100% zinc extracts. Whereas elongated, properly shaped and evenly distributed cells were seen in the control (Fig. S2, ESI†) and HUVECs subjected to 20% extracts, cells treated with zinc extracts of the highest concentration analyzed herein formed characteristic, discontinuous clusters, indicating cytoskeletal reorganization and depolymerization.

Cell shrinkage was the main phenomenon occurring in HUVECs exposed to 100% extracts, regardless of whether the materials were processed by HE or HSE. This is reflected in a substantial drop in the cytoskeleton shrinkage ratio (as illustrated in Fig. 8), computed with respect to the extract-free, control group (according to our previous study[14]). As the overall process of cytoskeleton condensation is viewed as both a necessary and sufficient condition inducing apoptosis,[38] this parameter may serve as an indication of cell size changes that lead to cell death. Interestingly, no statistically significant differences in the cytoskeleton shrinkage ratio were noticed when cells were treated with extracts collected after a 24-hour incubation of the materials. This observation points to the fact that neither chemical composition, nor deformation-induced microstructure changes influence cell behavior. However, after a 48-hour material incubation, considerable alterations in cell size were triggered, particularly in response to 100% extracts. An especially wide distribution of the cytoskeleton shrinkage ratio values ought to be noted for the HSE-processed materials, with Zn–0.8Mg demonstrating the most pronounced deviations. This indicates variability in the cell response to the Zn–0.8Mg alloy as some cells had already undergone cell death while others maintained normal shape and size.

3.7. Cell viability

The MTT assay results, presented in Fig. 9, reveal a consistent pattern: higher extract concentrations correspond to lower cell viability, and longer incubation times result in increased cytotoxicity. This aligns well with the findings from the CLSM data analysis. Generally, 20% extracts from a 24-hour incubation did not lead to cytotoxic effects in HUVECs, while 100% extracts induced moderate cytotoxicity. Variations in cell viability between different materials (HE *vs.* HSE; pure zinc *vs.* alloyed) were observed only for the Zn–0.8Mg HSE alloy (100% extract), suggesting a potential positive role of magnesium alloying and HSE processing (note the lack of statistical significance between 100% extracts of Zn HE and Zn–0.8Mg HE). However, the differences in cytotoxicity between HE and HSE extracts after a 48-hour incubation were less clear. The results might have been influenced by the dilution, as no statistical significance was found between any of the probes for 100% extracts.

3.8. Free radical formation

Due to difficulties in establishing a relationship between material composition or microstructure and cell response, diamond-based quantum sensing was introduced as a tool for cytotoxicity

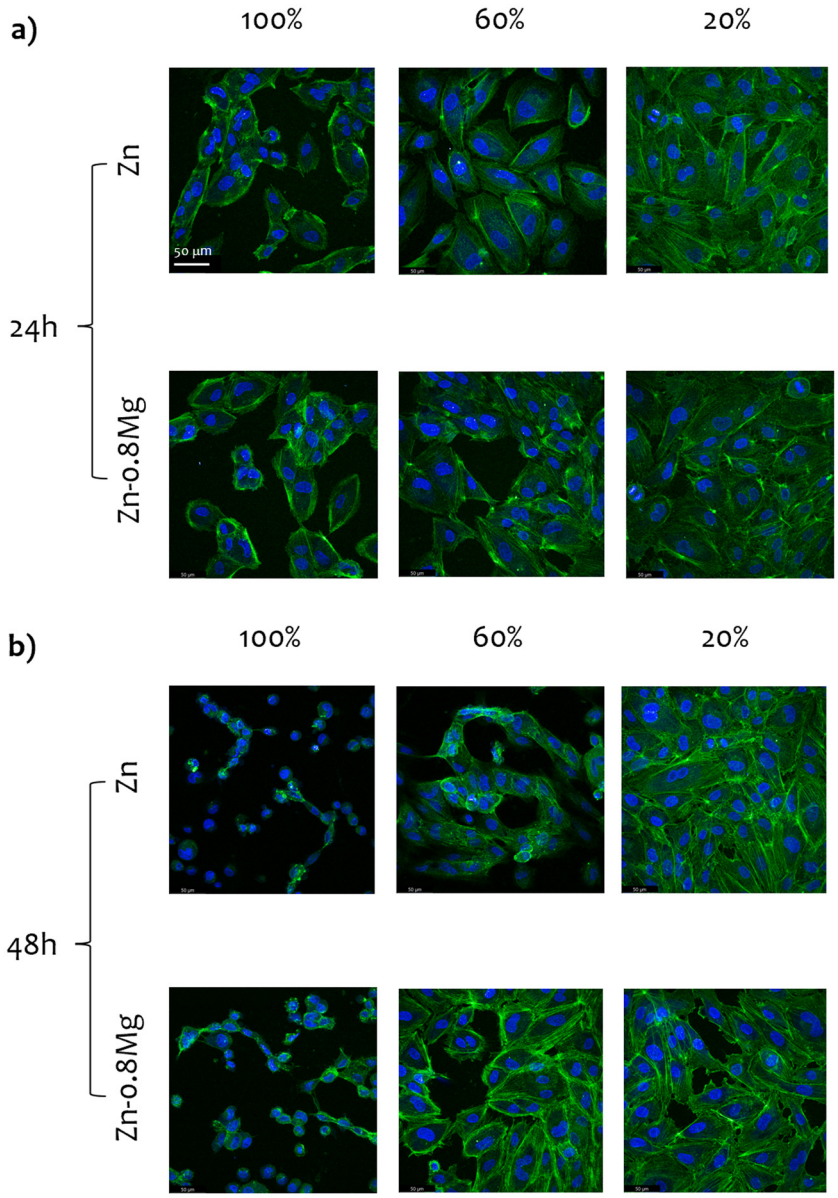

Fig. 6 CLSM-derived morphology of HUVECs treated with zinc extracts produced from HE-treated materials incubated in endothelial cell culture medium for (a) 24, (b) 48 hours. The scale bar in the Zn 100% 24 hours image is 50 μm and remains consistent across all images.

analysis. The results of T1 relaxometry studies (Fig. 10) were exclusively conducted on HUVECs exposed to extracts produced upon a 24-hour material incubation. This time point was selected due to the lack of discrepancies in cell morphology triggered by the extracts of varying content, alongside discernible differences in cell viability between Zn HSE and Zn–0.8Mg HSE. Irrespective of the extract concentration, the increased (in comparison to the extract-free control) production of free radicals was confirmed for all the investigated cultures. Alloying with magnesium and subsequent HSE processing indirectly led to greater free radical production in endothelial cells compared to unalloyed zinc processed by HSE. Conversely, no such correlation was found for the HE-treated materials as the differences in relaxation times between the Zn HE and the Zn–0.8Mg HE were never statistically significant across extract concentrations. These two findings indicate that when Zn is alloyed with Mg, processed *via* HSE, and subsequently exposed to EBM, the resulting extracts induce notable oxidative stress in endothelial cells. This claim is supported by the observation that 20% and 100% extracts of the Zn–0.8Mg HE resulted in reduced radical species formation compared to the Zn–0.8Mg HSE. The fact that regardless of the extract concentration, no statistical significance in relaxation times was recorded for HUVECs treated with the HE extracts implies that consistent levels of free radicals are generated in those cells.

Overall, T1 relaxometry studies revealed that alloying with magnesium and consequent HSE processing results in an elevated generation of radical species in HUVECs. However,

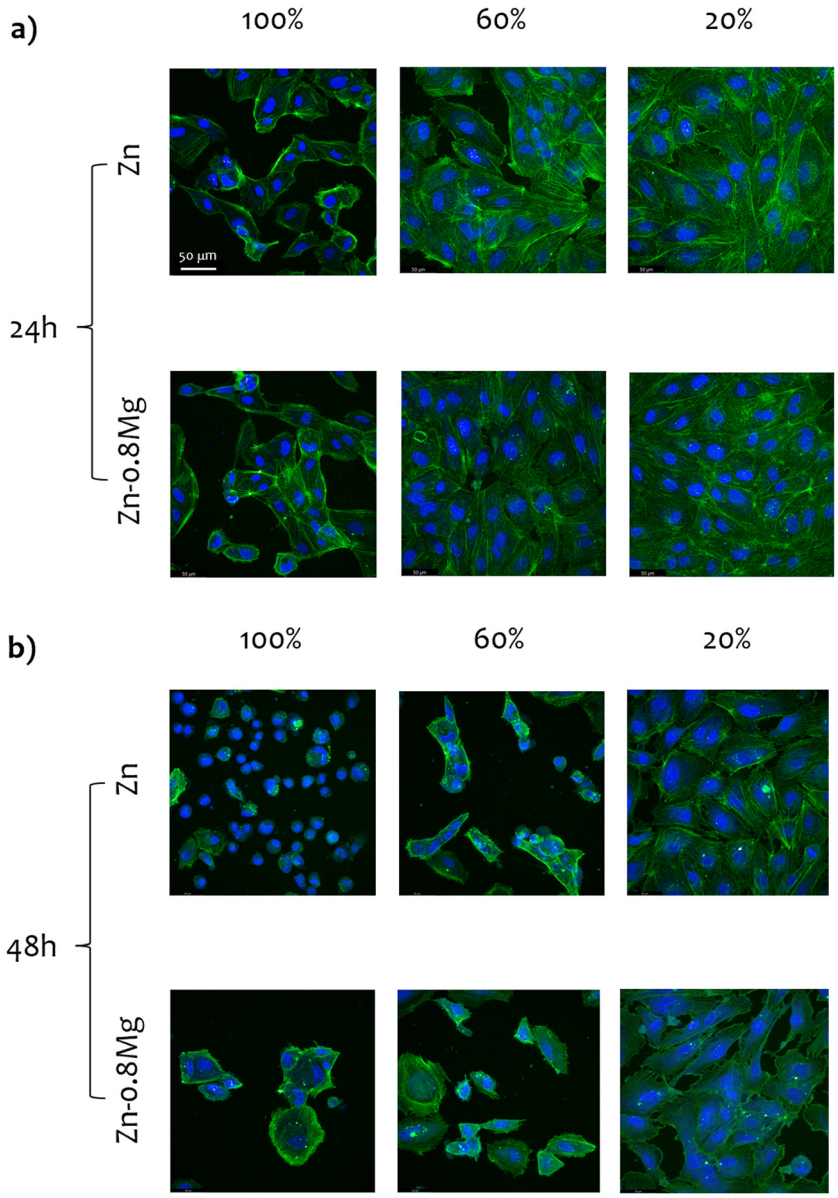

Fig. 7 CLSM-derived morphology of HUVECs treated with zinc extracts produced from HSE-treated materials incubated in endothelial cell culture medium for (a) 24, (b) 48 hours. The scale bar in the Zn 100% 24 hours image is 50 μm and remains consistent across all images.

one has to bear in mind that T1 relaxometry reveals the information at the nanoscale and that some free radicals exert a positive impact on endothelial cells, as discussed later. Interestingly, when HUVECs were treated with the 100% Zn HSE extracts, the intracellular generation of radical species was lower compared to the 100% Zn HE, and remained within the range of extract-free, untreated cells (naturally producing a variety of free radicals under normal physiological conditions).

4. Discussion

Biodegradable Zn–*x*Mg alloys have become one of the most commonly studied zinc-based materials in recent years. When Zn is alloyed with Mg, the formation of intermetallic phases takes place, which significantly contributes to an increase in the mechanical strength of the base material.[39] Hydrostatically extruded zinc and its alloys have demonstrated great potential as candidates for biodegradable implants due to their extraordinary mechanical properties.[9–11] For instance, a Zn–1Mg alloy, subjected to HSE in four consecutive stages, reached the yield strength (YS) of 383 MPa, the ultimate tensile strength (UTS) of 482 MPa and an elongation (*E*) of 23%. These values significantly surpass the design criteria for a new family of biodegradable stents.[11,40] By varying the Mg content, it was possible to accomplish higher strength or superior plasticity of the HSE-treated Zn-based materials. With just 0.5 wt% of Mg, the UTS of 517 MPa was achieved, although the elongation

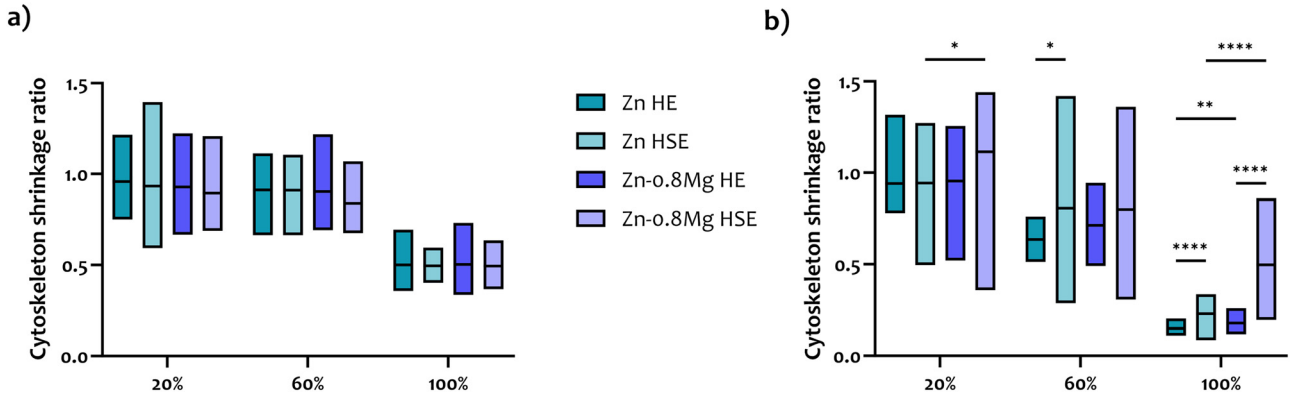

Fig. 8 Cell shrinkage ratio computed for HUVECs treated with zinc extracts collected upon (a) 24-hour, (b) 48-hour incubation of materials with endothelial cell culture medium. Data are presented as mean ± standard deviation. The asterisks denote statistical significance (*$p < 0.05$, **$p < 0.01$, ***$p < 0.001$, ****$p < 0.0001$).

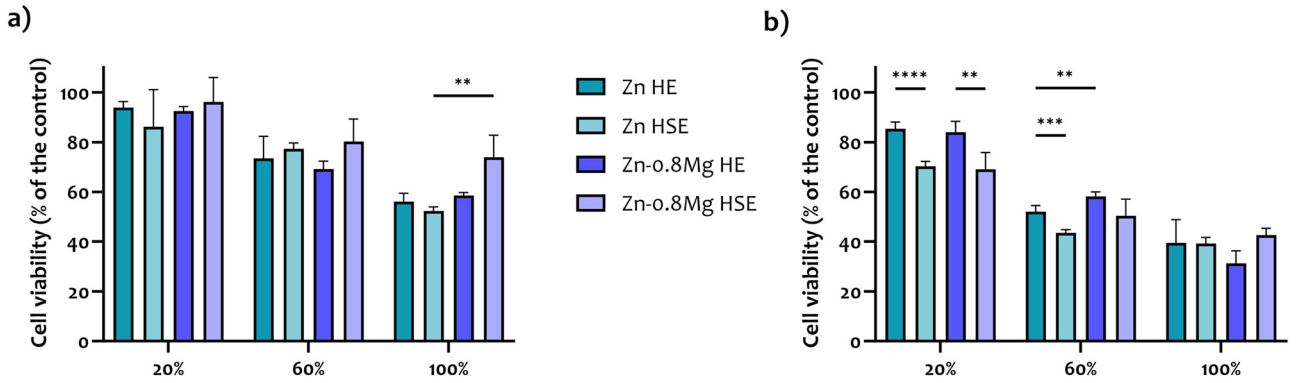

Fig. 9 Viability of HUVECs treated with zinc extracts collected from samples incubated with endothelial cell culture medium for (a) 24 hours; (b) 48 hours. Data are presented as mean ± standard deviation. The asterisks denote statistical significance (*$p < 0.05$, **$p < 0.01$, ***$p < 0.001$, ****$p < 0.0001$).

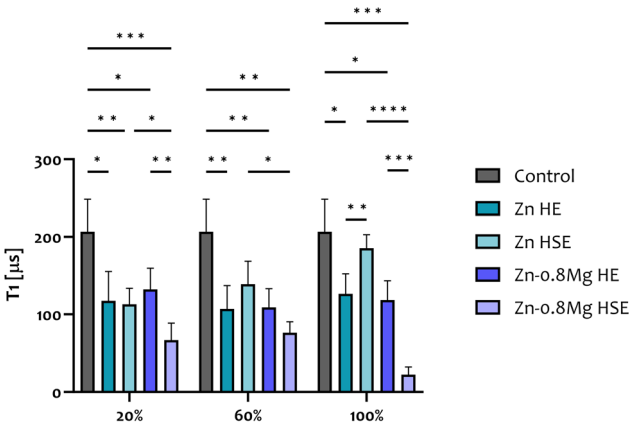

Fig. 10 Relaxation time charts obtained after a 4-hour incubation of HUVECs with zinc extracts produced within 24 hours of incubation of materials with endothelial cell culture medium. The experiments were performed in six replicates for each variant. Data are presented as means ± standard deviation. The asterisks denote statistical significance (*$p < 0.05$, **$p < 0.01$, ***$p < 0.001$, ****$p < 0.0001$).

decreased to 8%. Conversely, for the Zn–1.5Mg alloy processed in the same manner, the UTS decreased to 472 MPa while E increased to 38%. Therefore, to ensure a combination of both high strength and plasticity, a concentration of 0.8 wt% was proposed in this work. Additionally, from an economic standpoint, the number of HSE passes was reduced to 3, yet the mechanical performance (the UTS of 375 MPa, the E of 35%) was not hampered.[27]

Knowing that HSE zinc-based materials fulfill the mechanical requirements for medical applications, we proceeded with a comprehensive characterization of their cytocompatibility. In doing so, a novel method of T1 relaxometry has been utilized. Henceforth, we discuss the cytotoxicity of Zn–xMg alloys, with a focus on zinc processed by severe plastic deformation (SPD) processes. As HSE is considered an unconventional SPD process, we aimed to verify whether plastic deformation somehow affects the biodegradation of zinc-based materials and subsequent cell behavior. However, it needs to be borne in mind that, due to the degradability of zinc and its alloys, our observations are mostly of a speculative nature.

4.1. *In vitro* cytotoxicity of the Zn–xMg alloys

Magnesium has been preferred as an alloying addition for zinc owing to its immense biological significance.[41] Numerous studies have investigated the cytotoxicity of Zn–xMg alloys

using various cell cultures, including human osteosarcoma cells (U2-OS), human osteoblast cells, or fibroblasts (L929).[42–44] In general, an acceptable cell response has been reported. However, it has often been noted that cell activity may increase when cells are cultured with lower zinc concentrations, highlighting the relationship between the degradation rate of zinc-based materials and cytotoxicity.

Due to the usage of various cell lines, culture media, alloy compositions, incubation times for the preparation of extracts, and different assays for cytotoxicity evaluation, it is difficult to draw a uniform conclusion on the biocompatibility of the Zn–*x*Mg alloys. Still, considering the potential application of zinc as a vascular implant material, it is important to study how endothelial cells are affected by Zn and its alloys. One of the first studies addressing this issue was reported by Ma *et al.*[45] The authors demonstrated that zinc ions at low concentrations (20–60 μM) tend to stimulate HUVEC viability, proliferation, adhesion, spreading, and migration, as well as cytoskeletal reorganization. Inhibitory effects were observed when cells were treated with higher concentrations of Zn^{2+} (80–140 μM). The findings have become a major breakthrough in comprehending cell-biodegradable zinc interactions. However, the authors tested solutions of variously concentrated $ZnCl_2$, not ions released from biodegradable metallic samples into culture media.

Lin *et al.*[46] investigated how the Zn–0.02Mg alloy manufactured by HE influences HUVECs. The extracts taken from the incubated material promoted cell viability, especially after 1 day of treatment. This was further supported by cell morphology analysis, as HUVECs exposed to the Zn–0.02Mg extracts exhibited a typical cobblestone-like shape. On top of that, the authors showed that pure zinc extracts slightly reduced cell viability but did not induce cytotoxic responses. The results of this study contradict our findings, as we have shown that, regardless of the material composition, 60% and 100% zinc extracts caused moderate cytotoxicity.

To our best knowledge, there has been so far only one report addressing the impact of plastically deformed zinc on cell viability, *i.e.*, the study by Shen *et al.*[47] The authors tested extracts collected from the as-cast and as-extruded zinc as well as the Zn–1.2Mg alloy. They showed that osteosarcoma cells do not survive in extraction media with high ion concentration (50–100% for as-cast Zn–1.2Mg and 25–100% for as-extruded Zn–1.2Mg). On the other hand, the viability of MG-63 fibroblasts increased once 25% and 50% zinc extracts were used to culture cells. The negative impact of plastic deformation on cell viability was also emphasized and ascribed to the superior corrosion rate of the alloy, resulting in higher amounts of Zn^{2+} in the extracts. The results of this study do not coincide with our findings because, compared to the Zn–0.8Mg HE, the Zn–0.8Mg HSE experienced lower mass change upon immersion in EBM, unusual cell behavior (both cell death and cell survival), and the greatest production of intracellular free radicals. The reason behind these discrepancies appears to be the corrosion behavior, which, as discussed later, was more uniform and stable for the HSE materials.

Overall, since the current ISO standards for testing the cytotoxicity of materials may seem insufficient or even outdated for biodegradable materials (they were originally developed for non-degradable samples), we believe it is crucial to strive for novel protocols or make use of new methods for cytotoxicity screening. Within the present study, the nanoscale information obtained by employing T1 relaxometry, *i.e.*, the intracellular, local formation of free radicals in endothelial cells exposed to zinc extracts, complements the micro- and macroscale data gathered using the conventional MTT assay, and CLSM imaging, respectively.

4.2. Cytotoxicity at the nanoscale *via* T1 relaxometry

Recently, we revealed that the 100% and 50% zinc extracts (formed during a 24-hour incubation of the hot-extruded pure zinc with EBM) lead to the intracellular formation of free radicals in HUVECs, significantly affecting their behavior and morphology.[14] Within this study, we have shown that ions released from the materials deformed by HSE pose a threat to cell survival yet based on the cytotoxicity assay and cell morphology analyses, it may be stated that the changes were similar to these induced by materials produced *via* HE. However, the nanoscale information provided with T1 relaxometry revealed that cells subjected to the Zn–0.8Mg HSE extracts produced significantly greater amounts of free radicals compared to the Zn HSE and Zn–0.8Mg HE extracts. Free radical formation may affect cell behavior, either positively or adversely, and we believe the observed phenomena may result from a combination of the deformation mode, the extreme refinement of the intermetallic phase, and the consequent degradation behavior of the material. In fact, we have demonstrated that degradation of the alloys occurred mainly at the sites of the intermetallic phase enriched with magnesium. As a result, the extracts contained both Mg^{2+} and Zn^{2+}, which affected cell size, viability, and activity, including intracellular free radical generation.

Although zinc is considered a redox-inert element and does not directly participate in reduction–oxidation reactions, it may still mediate or trigger such reactions. Previously,[14] we explored some potential mechanisms linking an excess of zinc ions in cells to cell death. Our findings revealed that as the concentration of zinc extract increases, so does the concentration of zinc within cells, along with the levels of free radicals generated by cellular organelles. We hypothesized that the elevation of intracellular zinc ions, originating from endogenous sources, may prompt the release of Zn^{2+} ions from various protein sites, thereby triggering the production of reactive species. These processes ultimately result in an overload of free or labile zinc and subsequent cell death.

The fact that Mg and Zn promote the formation of free radicals has been confirmed by Jeong *et al.*[48] The study showcased prolonged reactive oxygen species (ROS) generation from a biodegradable hybrid comprised of a poly-*l*-lactic acid substrate with a Mg/Zn bilayer coating, suitable for stents. The authors revealed that degradation products continued to produce both superoxide and hydrogen peroxide seamlessly, even after the complete dissolution of the metallic films.

More importantly, the ability of biodegradable magnesium/zinc platform to generate measurable ROS in a simulated environment was demonstrated. The formation of free radicals has been viewed by authors as a beneficial event since some ROS not only tends to accelerate re-endothelialization but also minimizes the risk of in-stent restenosis. This is particularly notable for nitric oxide ($^{\bullet}$NO), which has a wide range of biological properties essential for maintaining vascular homeostasis.[49] Nitric oxide modulates vascular dilator tone, regulates local cell growth, and protects vessels from the injurious effects of platelets and cells circulating in the blood, thereby playing a crucial role in normal endothelial function. Within the present study, it may be hypothesized that the production of $^{\bullet}$NO contributes to the elevated free radical formation in cells exposed to the Zn–0.8Mg HSE extracts. In fact, despite the greatest free radical production, no drastic changes in cell viability and morphology were observed between HUVECs exposed to the Zn–0.8Mg HSE extracts and other zinc-containing media.

4.3. The effect of degradation behavior on material cytotoxicity

Investigating the biological response of biodegradable metals should be backed up by the examination of their corrosion properties. Herein, a meticulous analyses encompassing ion concentration, mass change, and electrochemical tests have been carried out. Generally, as the immersion time increased, so did the Zn^{2+} concentration in extracts. A decrease in the Zn^{2+} and Mg^{2+} concentration was observed only for the Zn–0.8Mg HE, suggesting the formation of complex corrosion layers/products. However, the irregular distribution of corroded pits over the HE material surfaces indicates that the corrosion layer has a less protective character. The HSE materials degraded more uniformly as confirmed by low variability in the values of mass change upon 24- and 48-hour immersion as well as homogeneous distribution of corrosion products on the surfaces. These observations imply that plastic deformation influences the corrosion behavior of materials and that the process of degradation for non-deformed materials may be heterogeneous due to the fact that the corrosion layers/products form, dissolve and release various ions to the corrosive media.

The potentiodynamic tests coincided with the analysis of mass change and ion concentration. For the HSE materials, upon incubation with HBSS, a solid, well-developed corrosion layer was present, and the differences in corrosion rates measured for samples after 1 and 30 days of immersion were marginal. In the case of the HE materials, the corrosion current densities and degradation rates increased substantially. Such heterogeneous corrosion behavior could be related to the coarse-grained microstructure with randomly distributed intermetallic phase. In fact, the size and distribution of both grains and second phases may be factors considerably affecting the corrosion properties of materials.[36,50] Due to the differences in electrochemical potential between the matrix and the intermetallic phase, galvanic couples may be created to rapidly initiate corrosion. Hence, at phase boundaries, the dissolution of the material and ion release to the EBM should be more pronounced, eventually affecting cell behavior.

Despite the fact that the HSE and HE materials differed greatly in terms of corrosion properties, their use for biological characterization did not reveal any strong tendencies. No striking discrepancies in cell morphology or viability were observed either upon extract dilution or with prolonged immersion time. However, cytotoxicity screening was performed by using variously concentrated extracts, rather than bulk specimens. As the name indicates, biodegradable samples tend to dissolve in specific environments, thus under biological conditions it becomes impossible, *e.g.*, to seed the cells directly onto materials. The ambiguity of the cytocompatibility results should be attributed to the microstructural heterogeneity of the HE-treated materials. We have continuously shown that plastically deformed samples, as opposed to the coarse-grained ones, are characterized by the abundance of corrosion initiation sites, mostly in the regions of the intermetallic phase. Degradation behavior is influenced by various surface imperfections and microstructural defects, therefore these factors can significantly impact the overall corrosion rate/mode of the material. The microstructural homogeneity and uniform distribution of intermetallic phases in plastically deformed samples may result in somehow controllable corrosion, further dictating the degradation process and potentially improving the material's performance in biomedical applications. Contrarily, degradation of non-deformed, coarse-grained materials is heterogeneous, thus localized corrosion takes place, leading finally to inconclusive cell response.

4. 4. Summary and future directions

Zinc-based alloys processed by various plastic deformation processes remain one of the most promising biodegradable materials for stents. In principle, SPD strengthens metals, alloys, and composites remarkably, yet microstructural changes may put cytocompatibility at risk. Herein, we have demonstrated that when zinc extracts formed during the incubation of materials processed by either HE or HSE are used for culturing of HUVECs, their viability decreases in a dose-dependent manner, as observed using the MTT assay and CLSM. Moreover, we have successfully applied T1 relaxometry to test whether zinc extracts may lead to the intracellular formation of free radicals. The nanoscale information provided with T1 relaxometry revealed that the HSE processing leads indirectly to more pronounced intracellular generation of free radicals in comparison to HE. Verifying these findings for materials obtained by other techniques, *e.g.*, ECAP or high-pressure torsion, would be especially beneficial to fully comprehend how plastic deformation affects the cell response to zinc and its alloys. A graphical scheme of the Zn–0.8Mg alloy degradation and its effect on endothelial cells is displayed in Fig. 11. Overall, it needs to be borne in mind that differences between various experiments *i.e.*, MTT, CLSM, and T1 originate from obtaining different types of information, *i.e.*, mitochondrial activity, cell morphology, and free radical production. Furthermore, while MTT and CLSM provide in fact data derived

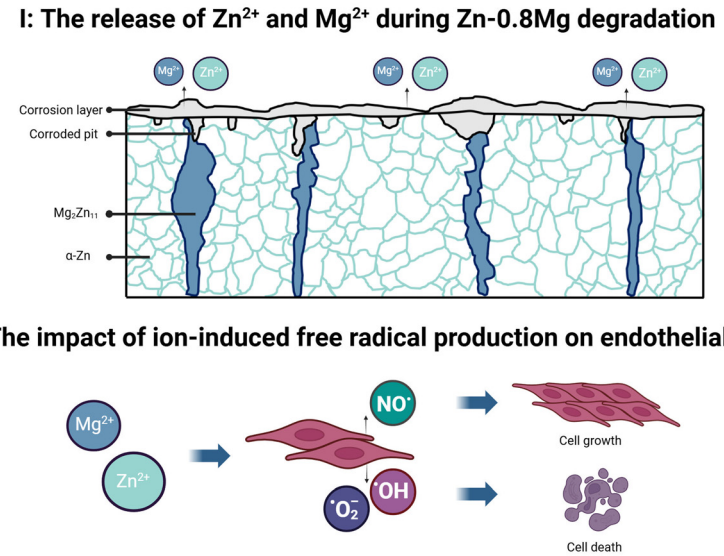

Fig. 11 A scheme depicting degradation of the Zn–0.8Mg alloy (viewed from the longitudinal cross-section of the material) and its postulated influence on endothelial cells. (I) The release of Zn^{2+} and Mg^{2+} during Zn–0.8Mg HSE degradation – as sample degrades, it is simultaneously covered with a corrosion layer, forms corroded pits, and releases ions into the medium. (II) The impact of ion-induced free radical production on endothelial cells: Zn^{2+} and Mg^{2+} are likely to mediate the elevated production of various free radicals in endothelial cells. These may have either adverse (*e.g.*, superoxide anion radical, hydroxyl radical) or positive (nitric oxide) impact. The former may lead to cell death, whereas the latter often results in the supported cell growth and vascular homeostasis.

from the microscale, T1 relaxometry is used to scan nanometric areas, therefore the results may vary considerably.

On top of that, all of the experiments described within the present study were conducted under static conditions, not reflecting the complexity of biological systems, including *e.g.*, blood flow, or the action of the immune system. Therefore, future studies in the area of biodegradable zinc and its alloys should involve examining cell responses under dynamic or at least quasi-dynamic conditions. The use of computational modeling, 3D/4D cell culturing, and *in vivo* trials is also recommended. As we have hypothesized that the elevated formation of free radicals in cells exposed to the Zn–0.8Mg HSE extracts may be associated with nitric oxide generation, the use of •NO-specific assays, such as diaminofluorescein-FM diacetate or 2,3-diaminonaphthalene is encouraged as well. In conclusion, we have shown that the Zn–0.8Mg alloy formed *via* HSE exhibits comparable cytocompatibility to the HSE-treated pure zinc. The only significant differences were observed upon performing the MTT assay for zinc extracts harvested after a 24-hour incubation of materials, and while carrying out T1 relaxometry measurements. We believe these phenomena may be attributed to the synergy of alloying and microstructural changes triggered by plastic deformation as well as subsequent biodegradation. The Zn–0.8Mg HSE alloy exhibited greater mass loss than the Zn HSE, and as degradation occurred at the regions of the intermetallic phase, the extracts used for culturing contained magnesium and zinc ions. However, the presence of both elements did not lead to drastic changes in the activity of HUVECs, apart from the greater production of intracellular free radicals.

5. Conclusions

In the present study, cytotoxicity analysis of two materials, pure zinc, and zinc alloyed with magnesium, processed *via* two different deformation routes, was carried out. Human umbilical vein endothelial cells were exposed to ions/particles/debris released during either 24- or 48-hour incubation of materials. The standard MTT assay was used for cytotoxicity screening, and confocal microscopy studies were performed to determine the alterations in cell morphology. Finally, T1 relaxometry, a novel quantum sensing technique, was implemented to determine if the intracellular formation of free radicals takes place in endothelial cells subjected to zinc media of varied content. The results of the experiments enabled to confirm that:

- Hydrostatic extrusion led to substantial microstructure refinement and even redistribution of the intermetallic phase in the matrix.
- Zn–0.8Mg alloys degraded more rapidly as compared with pure zinc, and the process of their degradation took place mainly in the areas of the intermetallic phase.
- The longer the zinc-based materials were incubated with a cell culture medium, the more inferior cell response they induced due to the higher content of Zn^{2+}/Mg^{2+} in the extracts.
- The viability of endothelial cells decreased with an increase in the concentration of zinc extracts used for culturing.
- Irrespective of the processing path, the material tested, or the duration of its incubation, zinc extracts of the highest concentration resulted in moderate cytotoxicity as manifested by cytoskeletal reorganization and depolymerization.
- No significant discrepancies in viability and morphology of endothelial cells were noted between HUVECs exposed to either

coarse-grained or plastically deformed materials, indicating that plastic deformation may not elicit a negative impact on cytocompatibility of the material.

• T1 relaxometry measurements confirmed the most elevated formation of intracellular free radicals in HUVECs exposed to the Zn–0.8Mg HSE extracts, though it could be speculated that these free radicals did not adversely affect cell function.

• The homogeneous microstructure of the HSE-treated materials, compared to their HE counterparts, could be responsible for the continuous release of Zn^{2+}/Mg^{2+} ions in a uniform manner, resulting in a higher concentration of intracellular free radicals.

• T1 relaxometry is a suitable tool for cytotoxicity analysis and it provides information from the nanoscale, complementary to the data obtained from cytotoxicity assays and microscopy-based cell morphology investigations.

Abbreviations

BSE	Backscatter electron
CLSM	Confocal laser scanning microscopy
DMSO	Dimethyl sulfoxide
EBSD	Electron backscatter diffraction
ECAP	Equal channel angular pressing
FND	Fluorescent nanodiamond
HAGB	High-angle grain boundary
HE	Hot extrusion
HSE	Hydrostatic extrusion
HUVEC	Human umbilical vein endothelial cell
LAGB	Low-angle grain boundary
NV	Nitrogen vacancy
PBS	Phosphate-buffered saline
ROS	Reactive oxygen species
SEM	Scanning electron microscopy
SPD	Severe plastic deformation

Conflicts of interest

None.

Acknowledgements

A.J. acknowledges financial support from National Centre for Research and Development, project no. LIDER/54/0229/L-11/19/NCBR/2020. R.S. acknowledges financial support from the European Commission *via* an ERC starting grant (ERC-2016-STG Stress Imaging 714289). The authors would like to thank the UMCG Endothelial Cell facility for providing the cells to be used for all cell response studies.

References

1 P. Libby, J. E. Buring, L. Badimon, G. K. Hansson, J. Deanfield, M. S. Bittencourt, L. Tokgözoğlu and E. F. Lewis, *Nat. Rev. Dis. Prim*, 2019, **5**, 56.
2 W. Jiang, W. Zhao, T. Zhou, L. Wang and T. Qiu, *Micromachines*, 2022, 13.
3 X. Chen, R. Chang, H. Liu, L. Zhang and Y. Zheng, *Bioact. Mater.*, 2023, **24**, 20–25.
4 R. B. Saper and R. Rash, *Am. Fam. Physician*, 2009, **79**, 768–772.
5 L. Kong, Z. Heydari, G. H. Lami, A. Saberi, M. S. Baltatu and P. Vizureanu, *Materials*, 2023, 16.
6 T. A. Vida, A. Conde, E. S. Freitas, M. A. Arenas, N. Cheung, C. Brito, J. de Damborenea and A. Garcia, *J. Alloys Compd.*, 2017, **723**, 536–547.
7 P. Sotoudeh Bagha, S. Khaleghpanah, S. Sheibani, M. Khakbiz and A. Zakeri, *J. Alloys Compd.*, 2018, **735**, 1319–1327.
8 C. Shuai, Y. Cheng, Y. Yang, S. Peng, W. Yang and F. Qi, *J. Alloys Compd.*, 2019, **798**, 606–615.
9 A. Jarzębska, M. Bieda, J. Kawałko, Ł. Rogal, P. Koprowski, K. Sztwiertnia, W. Pachla and M. Kulczyk, *Mater. Lett.*, 2018, **211**, 58–61.
10 A. Jarzębska, M. Bieda, Ł. Maj, R. Chulist, D. Wojtas, M. Strąg, B. Sułkowski, S. Przybysz, W. Pachla and K. Sztwiertnia, *Metall. Mater. Trans. A Phys. Metall. Mater. Sci.*, 2020, **51**, 6784–6796.
11 W. Pachla, S. Przybysz, A. Jarzębska, M. Bieda, K. Sztwiertnia, M. Kulczyk and J. Skiba, *Bioact. Mater.*, 2021, **6**, 26–44.
12 H. Kabir, K. Munir, C. Wen and Y. Li, *Bioact. Mater.*, 2021, **6**, 836–879.
13 A. Mzyk, A. Sigaeva and R. Schirhagl, *Acc. Chem. Res.*, 2022, **555**, 3572–3580.
14 D. Wojtas, R. Li, A. Jarzębska, B. Sułkowski, M. Zehetbauer, E. Schafler, K. Wierzbanowski, A. Mzyk and R. Schirhagl, *Adv. Quantum Technol.*, 2023, **2300174**, 1–13.
15 S. D. Pouwels, A. Sigaeva, S. de Boer, I. A. Eichhorn, L. Koll, J. Kuipers, R. Schirhagl, I. H. Heijink, J. K. Burgess and D. J. Slebos, *J. Mater. Sci.: Mater. Med.*, 2023, **34**, 38.
16 F. Perona Martínez, A. C. Nusantara, M. Chipaux, S. K. Padamati and R. Schirhagl, *ACS Sens.*, 2020, **5**, 3862–3869.
17 R. Sharmin, T. Hamoh, A. Sigaeva, A. Mzyk, V. G. Damle, A. Morita, T. Vedelaar and R. Schirhagl, *ACS Sens.*, 2021, **6**, 4349–4359.
18 N. Norouzi, A. Citra, Y. Ong, T. Hamoh, L. Nie, A. Morita, Y. Zhang, A. Mzyk and R. Schirhagl, *Carbon N. Y.*, 2022, **199**, 444–452.
19 K. Wu, T. A. Vedelaar, V. G. Damle, A. Morita, J. Mougnaud, C. Reyes San Martin, Y. Zhang, D. P. I. van der Pol, H. Ende-Metselaar, I. Rodenhuis-Zybert and R. Schirhagl, *Redox Biol.*, 2022, **52**, 102279.
20 L. Nie, A. C. Nusantara, V. G. Damle, M. V. Baranov, M. Chipaux, C. Reyes-San-Martin, T. Hamoh, C. P. Epperla, M. Guricova, P. Cigler, G. van den Bogaart and R. Schirhagl, *Nano Lett.*, 2022, **22**, 1818–1825.
21 Y. Tian, A. C. Nusantara, T. Hamoh, A. Mzyk, X. Tian, F. Perona Martinez, R. Li, H. P. Permentier and R. Schirhagl, *ACS Appl. Mater. Interfaces*, 2022, **14**, 39265–39273.
22 R. Sharmin, A. C. Nusantara, L. Nie, K. Wu, A. Elias Llumbet, W. Woudstra, A. Mzyk and R. Schirhagl, *ACS Sens.*, 2022, **7**, 3326–3334.

23 N. Lin, K. Van Zomeren, T. Van Veen, A. Mzyk, Y. Zhang and X. Zhou, *ACS Cent. Sci.*, 2023, **9**, 1784–1798.
24 H. T. Li, R. Schirhagl, J. Eliveld, A. Hoek, A. Cantineau and A. Mzyk, *Diam. Relat. Mater.*, 2023, **140**, 110388.
25 L. Nie, A. C. Nusantara, V. G. Damle, R. Sharmin, E. P. P. Evans, S. R. Hemelaar, K. J. van der Laan, R. Li, F. P. Perona Martinez, T. Vedelaar, M. Chipaux and R. Schirhagl, *Sci. Adv.*, 2021, **7**, eabf0573.
26 C. Reyes-San-Martin, T. Hamoh, Y. Zhang, L. Berendse, C. Klijn, R. Li, A. E. Llumbet, A. Sigaeva, J. Kawałko, A. Mzyk and R. Schirhagl, *ACS Nano*, 2022, **16**, 10701–10710.
27 A. Jarzębska, M. Gieleciak, A. Bigos, Ł. Maj, K. Trembecka-Wójciga, M. Bugajska, M. Bieda, Ł. Rogal, J. Kawałko, S. Przybysz, D. Wojtas, A. Mzyk and R. Schirhagl, *J. Mater. Res. Technol.*, 2024, **30**, 283–294.
28 O. A. Shenderova, A. I. Shames, N. A. Nunn, M. D. Torelli, I. Vlasov and A. Zaitsev, *J. Vac. Sci. Technol., B*, 2019, **37**, 30802.
29 S. R. Hemelaar, B. Saspaanithy, S. R. M. L'Hommelet, F. P. Perona Martinez, K. J. van der Laan and R. Schirhagl, *Sensors*, 2018, **18**, 355.
30 D. Wojtas, A. Mzyk, J. Kawałko, G. Imbir, K. Trembecka-Wójciga, M. Marzec, A. Jarzebska, L. Maj, K. Wierzbanowski, R. Chulist, W. Pachla and K. Sztwiertnia, *ACS Biomater. Sci. Eng.*, 2021, **7**, 114–121.
31 D. Wojtas, Ł. Maj, K. Wierzbanowski, A. Jarzębska, R. Chulist, J. Kawałko, K. Trembecka-Wójciga, M. Bieda-Niemiec and K. Sztwiertnia, *Arch. Civ. Mech. Eng.*, 2023, **23**, 9.
32 I. AAT Bioquest, Quest CalculateTM HBSS (Hank's Balanced Salt Solution) Preparation and Recipe, **https://www.aatbio.com/resources/buffer-preparations-and-recipes/hbss-hanks-balanced-salt-solution**, (accessed 25 April 2024).
33 A. Morita, T. Hamoh, F. P. Perona Martinez, M. Chipaux, A. Sigaeva, C. Mignon, K. J. van der Laan, A. Hochstetter and R. Schirhagl, *Nanomaterials*, 2020, **10**, 516.
34 E. Mostaed, M. Sikora-Jasinska, A. Mostaed, S. Loffredo, A. G. Demir, B. Previtali, D. Mantovani, R. Beanland and M. Vedani, *J. Mech. Behav. Biomed. Mater.*, 2016, **60**, 581–602.
35 M. M. Alves, T. Prošek, C. F. Santos and M. F. Montemor, *RSC Adv.*, 2017, **7**, 28224–28233.
36 L. Ye, H. Huang, C. Sun, X. Zhuo, Q. Dong, H. Liu, J. Ju, F. Xue, J. Bai and J. Jiang, *J. Mater. Res. Technol.*, 2022, **16**, 1673–1685.
37 J. Pinc, A. Školáková, V. Hybášek, Š. Msallamová, P. Veřtát, P. Ashcheulov, M. Vondráček, J. Duchoň, I. McCarroll, M. Hývl, S. Banerjee, J. Drahokoupil, J. Kubásek, D. Vojtěch and J. Čapek, *Bioact. Mater.*, 2023, **27**, 447–460.
38 N. J. Ernest, C. W. Habela and H. Sontheimer, *J. Cell Sci.*, 2008, **121**, 290–297.
39 X. Zhuo, Y. Wu, J. Ju, H. Liu, J. Jiang, Z. Hu, J. Bai and F. Xue, *J. Mater. Res. Technol.*, 2022, **17**, 244–269.
40 E. Mostaed, M. Sikora-Jasinska, J. W. Drelich and M. Vedani, *Acta Biomater.*, 2018, **71**, 1–23.
41 J. Venezuela and M. S. Dargusch, *Acta Biomater.*, 2019, **87**, 1–40.
42 J. Kubásek, I. Pospíšilová, D. Vojtěch, E. Jablonská and T. Ruml, *Mater. Tehnol.*, 2014, **48**, 623–629.
43 M. S. Dambatta, N. S. Murni, S. Izman, D. Kurniawan, G. R. A. Froemming and H. Hermawan, *Proc. Inst. Mech. Eng. Part H J. Eng. Med.*, 2015, **229**, 335–342.
44 H. Gong, K. Wang, R. Strich and J. G. Zhou, *J. Biomed. Mater. Res. – Part B Appl. Biomater.*, 2015, **103**, 1632–1640.
45 J. Ma, N. Zhao and D. Zhu, *ACS Biomater. Sci. Eng.*, 2015, **1**, 1174–1182.
46 S. Lin, X. Ran, X. Yan, Q. Wang, J. G. Zhou, T. Hu and G. Wang, *J. Mater. Sci.: Mater. Med.*, 2019, **30**, 12.
47 C. Shen, X. Liu, B. Fan, P. Lan, F. Zhou, X. Li, H. Wang, X. Xiao, L. Li, S. Zhao, Z. Guo, Z. Pu and Y. Zheng, *RSC Adv.*, 2016, **6**, 86410–86419.
48 G. Jeong, H. W. Hwang, M. Chae, S. H. Hong, J. Park, Y. Han, H. Jeon, Y. C. Kim, S. K. Kang, H. W. Jang, J. Y. Sun and M. R. Ok, *Langmuir*, 2022, **38**, 8003–8011.
49 D. Tousoulis, A.-M. Kampoli, C. Tentolouris Nikolaos Papageorgiou and C. Stefanadis, *Curr. Vasc. Pharmacol.*, 2011, **10**, 4–18.
50 T. Huang, Z. Liu, D. Wu and H. Yu, *J. Mater. Res. Technol.*, 2021, **15**, 226–240.